CrossMark
click for updates

In situ fabrication of (Sr,La)FeO$_4$ with CoFe alloy nanoparticles as an independent catalyst layer for direct methane-based solid oxide fuel cells with a nickel cermet anode†

Hong Chang,[a] Huili Chen,*[a] Zongping Shao,[b] Jing Shi,[c] Jianping Bai[d] and Si-Dian Li[a]

An independent catalyst layer is applied to develop a highly effective way to reduce coking when operating in methane based fuels, in which the catalyst layer is separated from a Ni cermet anode. In this way, Ni cermet anode conductivity is not influenced, and cell cracking due to the thermal–mechanical stress from the mismatched thermal expansion coefficients (TECs) between the catalyst and anode materials, the temperature gradients within the anode caused by the highly endothermic reforming reaction of methane, and the large internal strain during the reduction process is also avoided. La$_{0.6}$Sr$_{0.4}$Co$_{0.2}$Fe$_{0.8}$O$_{3-\delta}$ (LSCF), which is co-pressed with an Al$_2$O$_3$ substrate into a double-layered slice with a mesoporous structure, functions as an independent catalyst layer of the Ni-based anode. Under SOFC operating conditions, a K$_2$NiF$_4$-type oxide (Sr,La)FeO$_4$ with homogeneously dispersed CoFe alloy nanoparticles is formed, which shows good catalytic activity for methane partial oxidation with 88% conversion at 950 °C in a mixture of CH$_4$ and O$_2$ (1 : 1). A conventional cell with the state-of-art Ni cermet anode (NiO–8% Y stabilized ZrO$_2$ (YSZ)/YSZ/La$_{0.8}$Sr$_{0.2}$MnO$_3$–YSZ) is constructed and the electrochemical performance of cells with and without the independent catalyst layer is tested. In wet methane, the voltage of the conventional cell without the catalyst layer declines rapidly from 0.7 V to 0.1 V within 20 min at 333 mA cm^{-2} and 800 °C. In contrast, the voltage of the modified cell with an independent catalyst layer stabilizes at 0.79 V with negligible degradation within 116 h. In wet coal bed methane (CBM), the voltage of the modified cell with an independent catalyst layer exhibits a slow decrease from 0.69 V to 0.66 V within 12 h. The stable power output of the cell with an independent catalyst layer under a constant current load in methane indicates excellent coking resistance. The microstructure and surface composition of the catalyst layer and anode are further analyzed by SEM and EDX after the stability test.

Introduction

Solid oxide fuel cells (SOFCs), which operate at 500–1000 °C, can convert the chemical energy stored in a fuel to electric power through electrochemical reactions with high efficiency and low emissions. The high-temperature operation allows for the use of a variety of fuels in addition to hydrogen (H$_2$), such as solid carbon,[1–3] natural gas,[4] synthesis gas[5] and other hydrocarbons.[6–11] Nickel-based cermets like Ni–YSZ are the state-of-the-art anode materials for SOFCs because of their high catalytic activity for H$_2$ and hydrocarbon electro-oxidation, low cost and high electrical/thermal conductivity. Unfortunately, metallic nickel also has good catalytic activity for C–H bond dissociation; consequently, carbon deposition over the nickel surface happens easily when hydrocarbons are employed as the fuels, which could result in quick deactivation in cell performance or even failure of fuel cells with conventional nickel-based anodes.

A number of approaches have been tried to mitigate or eliminate carbon deposition over the Ni-based anodes when hydrocarbon-based fuels are used directly, such as alloying Ni in the anode with other elements,[12–16] modifying the Ni surface with some oxides,[17–20] developing Ni-free metal anodes[21,22] or applying oxide-based anodes,[23–28] which have been reviewed by Wang *et al.*[29] Internal reforming of hydrocarbon fuels to syngas

[a]Institute of Molecular Science, Shanxi University, Key Lab Mat Energy Convers & Storage Shanxi Prov, Taiyuan 030006, People's Republic of China. E-mail: huilichen@sxu.edu.cn

[b]State Key Laboratory of Materials-Oriented Chemical Engineering, College of Chemistry & Chemical Engineering, Nanjing University of Technology, No. 5 Xin Mofan Road, Nanjing 210009, PR China

[c]Analytical Instrumentation Center, Institute of Coal Chemistry, Chinese Academy of Sciences, 27 South Taoyuan Road, Taiyuan 030001, PR China

[d]State Key Laboratory of Coal and CBM Co-ming, Shanxi Lanyan Coalbed Methane Group Co. Ltd, Jincheng 048204, PR China

† Electronic supplementary information (ESI) available. See DOI: 10.1039/c6ta04639h

has turned out to be an effective and facile way of reducing coke formation over the nickel anode of conventional SOFCs since nickel is much less susceptible to coke formation under a CO atmosphere than hydrocarbons. By employing an efficient catalyst in the anode chamber,[16,19] which can be deposited directly over the anode surface to form a functional layer or located near the anode surface, significant improvement in cell operation stability can be achieved because hydrocarbon fuels should first pass through the catalyst layer before reaching the anode layer. In this way, the concentration of the hydrocarbon inside the anode layer is minimized and coking on the anode is avoided. However, direct deposition of the catalyst over the anode surface would not only increase Ni cermet anode resistance, but also would cause cell cracking due to the mismatch of thermal expansion coefficients (TECs) between the catalyst and anode materials and the large internal strain during the reduction process. In addition, the high heat absorbed in the endothermic hydrocarbon reforming reactions also causes local temperature variation across the anode which leads to cell cracking due to the thermal–mechanical stress.[30–32] Pillai reported that the application of chemically inert PSZ anode barrier layers reduced the temperature gradients across the anode due to the decreased catalytic reforming rate, thereby enhancing cell stability.[32] Therefore, an independent active catalyst layer is more preferable owing to the following three advantages. First, CH_4 conversion is improved so that carbon deposition can be reduced; second, cell resistance is not influenced; third, thermal gradients can be reduced.

Ultrafine metallic nickel/cobalt (typically realized through supporting on a substrate) has also been demonstrated to be a superior catalyst for oxidation/reforming of hydrocarbons.[14,33,34] The formation of alloys is also found to be an effective way for reducing coking over nickel based catalysts.[8,14,35,36] Composite anodes containing Co–Fe alloy[21,37] or Ni–Fe alloy[12] nanoparticles have shown excellent electrochemical performance without coking. Methods commonly used to prepare alloy catalysts include the glycine nitrite process, Pechini, sol–gel and others. However, the catalyst powders prepared using these methods are unevenly dispersed with a larger particle size, which decreases the specific surface area and influences the catalytic activity of the catalyst. Another type of widely used method is impregnation in which the catalyst is deposited onto the anode layer. However, this process is time-consuming and uncontrollable over an even distribution of the infiltrated phase.

In recent years, the *in situ* fabrication method has been developed to prepare alloys with uniformly distributed nanoparticles.[12] In this method, the reducible elements which are doped into the perovskite are partly reduced and exsolved out of the lattice under a reducing atmosphere. $La_{0.6}Sr_{0.4}Co_{0.2}Fe_{0.8}O_{3-\delta}$ (LSCF) is one of the most popular perovskite-type cathode materials. Under a reducing atmosphere, LSCF could be reduced with the formation of a K_2NiF_4-type oxide $(Sr,La)FeO_4$ and CoFe alloy. Due to the homogeneous distribution of La, Sr, Co and Fe at the atomic level inside the LSCF oxide lattice, good dispersion of CoFe alloy within the K_2NiF_4-type $(Sr,La)FeO_4$ matrix could be achieved. The catalytic activity of the CoFe alloy

and the oxygen conductivity of the K_2NiF_4-type oxide provide the reduced LSCF with excellent catalytic activity for hydrocarbon oxidation/reforming,[38–40] which may be used as an internal reforming catalyst for SOFCs operating on hydrocarbon fuels.

As mentioned above, an independent catalyst layer would be a more preferable way to minimize the effect of the catalyst on the cell. In this study, we propose a double-layered catalyst slice which is composed of a LSCF catalyst layer and an Al_2O_3 substrate layer. Al_2O_3 was used to improve the mechanical strength. The catalyst slice was located close to but separated from the anode surface to function as a methane oxidation/reforming catalyst for SOFCs. Attractive cell power output and operational stability were demonstrated for the modified cell with an independent LSCF catalyst layer operating on methane and practical coal-bed methane (CBM), which exhibited an improvement over the conventional cell without the catalyst layer using a Ni–YSZ cermet anode. It provides an effective alternative way for the coking-free operation of SOFCs on practical hydrocarbon fuels without large modification of the fuel cell itself, thus bringing a wide application opportunity.

Experimental

Synthesis of LSCF perovskite

LSCF was synthesized *via* a combined ethylenediaminetetraacetic acid (EDTA)–citric acid (CA) complex method. According to the stoichiometric ratio of $La_{0.6}Sr_{0.4}Co_{0.2}Fe_{0.8}O_{3-\delta}$, the calculated quantities of nitrate compounds of La, Sr, Co and Fe ($La(NO_3)_3 \cdot 6H_2O$, $Sr(NO_3)_2$, $Co(NO_3)_2 \cdot 6H_2O$ and $Fe(NO_3)_3 \cdot 9H_2O$, respectively) were dissolved in ultrapure water at room temperature. The required amount of EDTA powder was dissolved in aqueous ammonia to obtain an $EDTA–NH_3 \cdot H_2O$ solution. The $EDTA–NH_3 \cdot H_2O$ solution and CA were added to the above aqueous nitrate solution in sequence with a molar ratio of M^{n+} : CA : EDTA controlled to be 1 : 2 : 1, then aqueous ammonia was added to the final solution to adjust the pH to $\sim$6–7. The final aqueous solution was heated with stirring to coordinate the metal ions. After removing excess water, a precursor gel formed, which was then heated for 8 h at approximately 250 °C. LSCF was obtained after calcination for 2 h at 1100 °C in air. The powder was characterized using X-ray diffractometry (XRD).

The preparation and N_2 adsorption/desorption isothermal experiments of the double-layered catalyst slice

A powder of polyvinyl butyral (PVB) and Al_2O_3 was mixed evenly at a mass ratio of 3 : 25. This powder (0.25 g) was pressed using a steel mold (13 mm diameter) at 144 MPa. Subsequently, 0.03 g powder that had been mixed uniformly with PVB and LSCF with a mass ratio of 12 : 5 was rolled out homogeneously over the substrate and co-pressed at 240 MPa to form a double-layered catalyst slice, which was then heat-treated at 900 °C for 4 h.

N_2 adsorption/desorption isothermal experiments were performed to investigate the pore properties of the double-layered catalyst slice. The isotherms were obtained using a Micromeritics ASAP-2020 M automated surface area and pore size

distribution analyzer (Micromeritics, USA) after degassing for 24 h at 200 °C under vacuum. N_2 adsorption isotherms were measured at 77 K using a conventional flow-type adsorption apparatus. The specific surface area of the sample was calculated using the multiple-point Brunauer–Emmett–Teller (BET) method. The pore size distributions and pore volume of the sample were calculated using the Barrett–Joyner–Halenda (BJH) method.

Cell fabrication

Nano-scale NiO was provided by the Chengdu Shudu Nanomaterials Technology Development Co., Ltd (Sichuan, China). YSZ and $La_{0.8}Sr_{0.2}MnO_{3-\delta}$ were purchased from the Ningbo Institute of Industrial Technology. NiO, YSZ and PVB (which functions as a pore-forming reagent and binder) with a mass ratio of 6 : 4 : 1 were ball-milled in ethanol for 1 h at 100 rpm. The slurry was heated gently and ground to form the anode powder. This powder (0.25 g) was placed into a steel mold (15 mm diameter) and was pressed at 110 MPa for 30 s to form an anode substrate. Subsequently, 0.025 g YSZ powder was rolled out homogeneously on the substrate surface and was co-pressed at 180 MPa to form an anode/electrolyte double-layered slice, which was then heat-treated at 1400 °C for 5 h. Lastly, the cathode paste $La_{0.8}Sr_{0.2}MnO_{3-\delta}$–YSZ was sprayed evenly on the electrolyte surface using a spray gun with an effective area of 0.48 cm^{-2}, followed by sintering at 1100 °C in air for 2 h. Silver paste was used to collect current from the cathode. Silver wires were extruded from the Ni cermet anode and LSM–YSZ cathode, respectively, to conduct current. This conventional cell without the catalyst layer is designated as "Ni–YSZ".

The following steps describe how the cell with a catalyst layer that was separated from the anode was fabricated. Firstly, the double-layered catalyst slice was fixed on the top of a test quartz tube using a small quantity of silver paste, and secondly, a button cell with a concave anode was fixed over the catalyst layer with the anode side towards the catalyst layer and was sealed using silver paste. The modified cell with the independent catalyst layer is designated as "LSCF//Ni–YSZ".

Characterization

XRD (Rigaku D/Max-RB, Japan) equipped with Cu Kα radiation was used for phase analysis with a diffraction angle 2θ from $10°$ to $80°$ (40 kV, 35 mA). The particle size was estimated from the (002) diffraction peak using the Debye–Scherrer equation. The cell surface morphologies and microstructure were characterized by SEM (JSM-7001F, JEOL, Japan) equipped with an energy-dispersive X-ray (EDX) spectrometer (Bruker, Germany).

The electrochemical performance of the cells was measured using an Iviumstat electrochemical workstation (Ivium Technologies B.V., Netherlands) from 750 to 850 °C. Before the cell test, hydrogen was applied to reduce the catalyst layer and NiO and maintained at 700 °C for 2 h. Hydrogen or 3% H_2O-humidified CH_4 or CBM flowed into the anode chamber at a constant flow velocity of 80 mL min^{-1} (standard temperature and pressure). After the fuel was fed to the anode, OCV was monitored until it was stable before the cell performance was

recorded. Surrounding air was used as the oxidant gas. The impedance spectra under open circuit and polarization conditions were collected with an amplitude of 10 mV from 1 MHz to 0.1 Hz. In general, the ohmic resistance (R_o) of the cell approximately equals the intercept of the impedance curve with the real axis in the high-frequency region. The difference of the impedance arc with the real axis corresponds to the polarization resistance (R_p), which is composed of an electrode polarization resistance (R_e) (corresponding to the high-frequency R_p) correlated with electrochemical reactions, and a diffusion resistance (R_d) (corresponding to the low-frequency R_p) that is associated with a mass transfer.

Catalytic activity test

The catalytic activity of the *in situ*-reduced LSCF powder for methane oxidation/reforming was evaluated using a flow-through fixed-bed quartz-tube reactor. Approximately 0.2 g of catalyst particles (40–60 mesh) was loaded in the middle of the reactor and was treated for 2 h with pure H_2. Then the reactants, CH_4/O_2 (1 : 1) or CH_4/H_2O (2 : 1) were introduced from the top of the tube with a CH_4 flow rate of 5 mL min^{-1} (standard temperature and pressure). Effluent gases were flowed out from the bottom of the tube and were introduced into an Agilent 7820 gas chromatograph for on-line gas compositional analysis. The instrument was equipped with a Hayesep Q, a Poraplot Q, a 5 Å sieve molecular column and a thermal conductivity detector for the separation and detection of CO, CO_2 and CH_4. The catalytic reactions for methane oxidation and steam reforming were performed in the range of 400–950 °C and 750–900 °C, respectively. The CH_4 conversion and CO selectivity were calculated using the approach described in our previous paper.[41]

Results and discussions

Mesoporous structure of the catalyst double-layered slice

The pore properties of the catalyst layer are strongly correlated with the catalytic activity and fuel gas transportation. Herein, the specific surface area and pore parameters of the LSCF–Al_2O_3 double-layered slice are determined using the adsorption of nitrogen at 77 K. The BET surface area is 67.6 m^2 g^{-1}. The BJH pore volume is 0.16 cm^3 g^{-1}. The adsorption/desorption isotherm exhibits a typical type-H3 hysteresis loop which starts from the relative pressures ($P/P_0 = 0.6$) and closes near $P/P_0 = 1$ (Fig. 1). This indicates a highly mesoporous structure with slit-shaped nanopores. The mesopore peak of the pore size distribution curve is intense and sharp with a mean pore diameter of *ca.* 10.1 nm, which is beneficial to gas transportation.

Structure and morphology of the cell with an independent catalyst layer

An illustration of the cell assembly with an independent catalyst layer, and the cross-sectional microstructures of the catalyst layer, anode, electrolyte and cathode are shown in Fig. 2. The catalyst layer is located close to the surface of the anode. Current is conducted by a silver wire from the Ni–YSZ anode and LSM–YSZ cathode. In this case the non-conducting catalyst
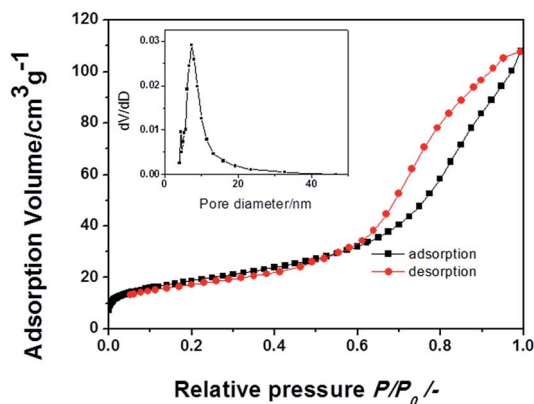
Fig. 1 Nitrogen gas adsorption/desorption isotherm for the catalyst layer. The inset is the pore size distribution of the sample.

would not affect the conductivity of the Ni-based anode. As is well known, oxygen (O_2) can eliminate carbon deposited on the anode. Therefore O_2 leakage from the electrolyte into the anode must be prevented in order to accurately evaluate the coking resistance of the anode. For this reason, a 33 μm thick and densified electrolyte layer is used in our work. No delamination is observed at the interface of the electrolyte with the anode and cathode. The catalyst layer is composed of 70 μm LSCF catalyst and 1.2 mm Al_2O_3 substrate. The double-layered catalyst layer, anode layer and cathode layer all exhibit high porosity, which ensures fuel gas supply and air circulation.

X-ray patterns of as-sintered and reduced LSCF

Fig. 3a presents the XRD pattern with Cu Kα radiation for the as-sintered powder heat-treated for 2 h in air at 1100 °C. The powder has a typical perovskite phase of $La_{0.6}Sr_{0.4}Co_{0.2}Fe_{0.8}O_3$, which agrees with those reported.[42–45] The average particle size of the powder is ∼20.2 nm as estimated by Scherrer's equation, which agrees with those reported by Ghouse *et al.*[29] for LSCF powders prepared by the sol–gel synthesis method. As expected, LSCF is unstable in a reducing atmosphere. After as-sintered LSCF was treated in pure hydrogen at 800 °C for 2 h, phase transition occurred. The corresponding XRD profile is shown in Fig. 3b. A K_2NiF_4-type oxide $(Sr,La)FeO_4$ (ICSD: 71-1744) and alloy Co_3Fe_7 (ICSD: 48-1817) are formed after treatment in hydrogen. This result matches that of Fe- and Co-based
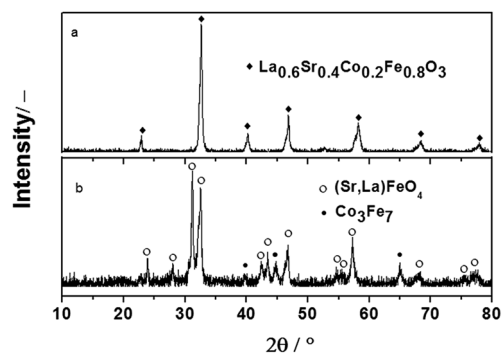

Fig. 3 X-ray patterns (XRD) of (a) as-sintered LSCF and (b) reduced powders.

perovskites which decompose to metal oxide and metal phases in reducing atmospheres.[46,47] Because the K_2NiF_4-type oxide $(Sr,La)FeO_4$ is oxygen conductive, it is believed that the decomposed products, $(Sr,La)FeO_4$ and the alloy Co_3Fe_7, would have good catalytic activity towards CH_4 oxidation.[37]

Catalytic activity of *in situ*-reduced LSCF towards methane oxidation and methane steam reforming

The K_2NiF_4-type oxide and CoFe alloy have been proved to be a superior catalyst for oxidation/reforming of hydrocarbons.[33,34,38–40] The CH_4 oxidation reaction, which occurs on metal oxides, consumes the surface lattice oxygen atoms and leads to the formation of surface O^- vacancies. Thus, if oxygen species, such as O_2 or water vapor, are present, they will be captured by O^- vacancies and be activated to react with CH_4. On the other hand, due to the existence of H_2O and CO_2 produced by H_2 and CO electrochemical reaction, probably methane steam/CO_2 reforming also occurs.

The catalytic performance of the *in situ*-reduced LSCF powder for methane oxidation (CH_4 : O_2, 1 : 1) and methane steam reforming (CH_4 : H_2O, 2 : 1) is tested in the range of 400–950 °C and 750–900 °C, respectively. Methane oxidation begins at 450 °C (Fig. 4a). Below 750 °C, the main carbonaceous product is CO_2. Above 750 °C, CO selectivity increases significantly with temperature. CH_4 conversion increases with temperature and reaches up to 88% at 950 °C with 69% CO selectivity. The high CH_4 conversion reveals that the reduced LSCF has a high catalytic reactivity for methane oxidation.
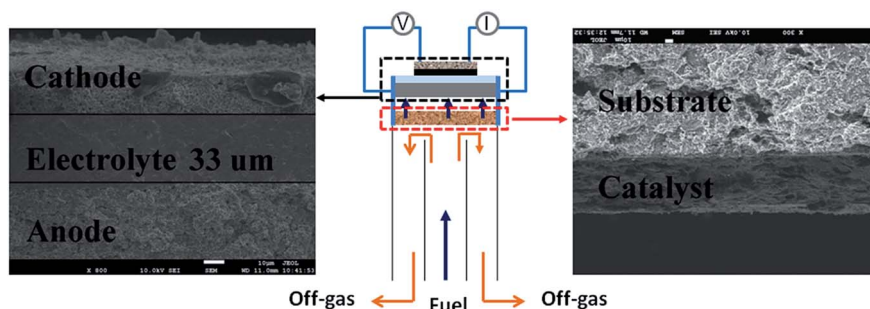

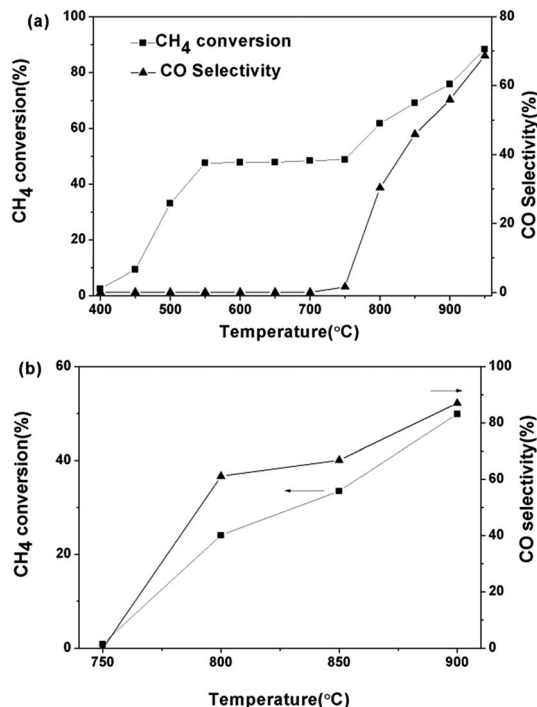**Fig. 2** Illustration of the cell with an independent catalyst layer.

Fig. 4 CH_4 conversion (■) and CO selectivity of *in situ*-reduced LSCF powders for methane oxidation (a) with a CH_4–O_2 (1 : 1) mixture in the range of 400 to 950 °C (▲) and for methane steam reforming (b) with a CH_4–H_2O (2 : 1) mixture in the range of 750 to 900 °C.

For steam reforming, methane conversion is almost zero at 750 °C. However, with increase in temperature, methane conversion and CO selectivity reach up to 49.9% and 86.9% at 900 °C (Fig. 4b), respectively, which indicates that the reduced LSCF has moderate catalytic activity for methane steam reforming at higher temperature. The above results indicate that the catalytic activity of the reduced LSCF for methane oxidation is higher than that for steam reforming. Under SOFC conditions, probably methane partial oxidation and steam/CO_2 reforming co-exist.

In order to better assess the application potential of (Sr,La)FeO$_4$ with CoFe alloy nanoparticles as an independent catalyst, it would be better to compare the methane reforming performance with other reported catalyst materials. However, it is difficult to directly compare the catalytic activities because of the different operation conditions in the reported papers. Methane conversion is related to many factors, such as the gas composition (S/C), temperature, gas flow rate, *etc.*[55] Usually, a larger S/C and higher temperature lead to higher methane conversion.[56] However, the higher H_2O content would dilute the fuel and oxidize the Ni particles on the SOFC anode, which decreases the cell performance. Selected recently reported papers on methane steam reforming related to SOFCs have been listed in Table 1 with their corresponding operation conditions.
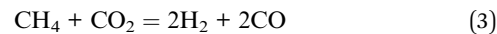
SOFC performance

It is expected that Ni-based SOFCs with *in situ* fabrication of (Sr,La)FeO$_4$ and CoFe alloy nanoparticles in an anode chamber would have a good coking resistance when wet methane-based fuels are used because fuels would be reformed to CO and H_2 before they reach the Ni-based anode. Because the catalyst layer also functions as a diffusion barrier layer, some unreformed methane would flow out along with the exhaust. In this case, the methane concentration over the anode layer would decrease significantly.

Excessive H_2O in fuels can inhibit carbon deposition by steam reforming (eqn (1)) or the carbon removal reaction (eqn (2)).

$$CH_4 + H_2O = 3H_2 + CO \qquad (1)$$

$$C + H_2O = H_2 + CO \qquad (2)$$
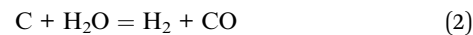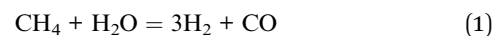
The thermodynamic threshold of the S/C ratio for preventing carbon formation is 2. However, high H_2O content in the fuel would dilute the fuel which causes low energy conversion efficiency. In addition, excess H_2O would cause oxidation of the Ni particles on the anode, which influences the electronic conductivity of the anode. In fact, H_2 electrochemical oxidation on the anode produces a large amount of H_2O, which can participate in CH_4 steam reforming and carbon removal reactions. CO_2, the product of CO electrochemical oxidation on the anode, is also favorable for CH_4 dry reformation by the reaction shown in eqn (3):

$$CH_4 + CO_2 = 2H_2 + 2CO \qquad (3)$$

The electrochemical performance of the modified cell in fuels containing different contents of H_2O at 850 °C was

Table 1 Comparison of the catalytic activities of selected catalysts toward methane steam reforming

Catalyst	CH_4–H_2O fuels (S/C)	CH_4 conversion, %	Temperature (°C)
LSCF (this work)	0.5	49.9	900
Ni–Cu/Ni–Fe alloys–BaZr$_{0.1}$Ce$_{0.7}$Y$_{0.1}$Yb$_{0.1}$O$_{3-\delta}$ (80 : 20 wt%)[48]	1	96.67	800
Ni–YSZ (57 : 43 wt%)[48]	1	62.98	800
0.5% Pt/12% CeO$_2$/α-Al$_2$O$_3$ (ref. 49)	3	80	800
Ni (45 wt%)–BaZr$_{0.7}$Ce$_{0.2}$Y$_{0.1}$O$_{2.9}$ (ref. 50)	2	45	550
Ru + Ni/LaPrMnCr/YSZ[51]	2	55	600
Ni–SDC–Ca (5 mol%)[52]	1	83.1	650
Ni–MnO (10%)/YSZ[53]	1	63	800
Ni/γ-Al$_2$O$_3$ (ref. 54)	3	88	655

This journal is © The Royal Society of Chemistry 2016

J. Mater. Chem. A, 2016, **4**, 13997–14007 | **14001**

investigated. The PPD continuously decreases with increasing H_2O content from 0.66 W cm^{-2} in 3% H_2O–97% CH_4 to 0.44 W cm^{-2} in 20% H_2O–80% CH_4 (Fig. S1†). Similarly R_o shows a slight increase with increasing H_2O content, probably due to the oxidation of Ni particles in the anode. However, R_p decreases when increasing the H_2O content from 3 mol% to 10 mol%, which is ascribed to the increased CH_4 conversion. With the H_2O content increasing to 20 mol%, R_p increases probably due to fuel dilution and the decreased temperature caused by the endothermic reaction of methane reforming. A similar changing trend of R_p with different H_2O contents in fuels was even observed by Hua, in which alloys reduced from $Ni_{0.5}Cu_{0.5}Fe_2O_4$ were used as methane catalysts for the Ni cermet anode.[13]

To evaluate the coking resistance ability of the cell with an independent catalyst layer, 3% H_2O–97% CH_4 and 3% H_2O–97% CBM (composition: CH_4, 82.9975%; O_2, 2.1853%; N_2, 10.1839%; C_2–C_8, 3.4731%; CO_2, 1.1602%) were fed into the cell. Fig. 5 shows the temperature-dependent polarization and power output of full cells with the Ni–YSZ anode in the absence (Fig. 5a and c) and presence (Fig. 5b and d) of the LSCF catalyst layer using wet CH_4 and wet CBM, respectively. The results indicate that the application of an independent catalyst layer improves the polarization performance of Ni–YSZ based cells at high temperature. For example, for the cell with the LSCF catalyst layer using CH_4 fuel [(LSCF//Ni–YSZ)-CH_4] (Fig. 5b), peak power density (PPD) is 0.66 W cm^{-2} at 850 °C, higher than 0.50 W cm^{-2} for the conventional cell without the catalyst layer [(Ni–YSZ)-CH_4] (Fig. 5a) at the same temperature. Similarly, for the cell with the LSCF catalyst layer using wet CBM

fuel [(LSCF//Ni–YSZ)-CBM] (Fig. 5d), peak power density (PPD) is 0.59 W cm^{-2} at 850 °C, higher than 0.55 W cm^{-2} for the conventional cell without the catalyst layer [(Ni–YSZ)-CBM] (Fig. 5c). However, with decrease of temperature, performance drop for the modified cell is more than that of the conventional cell. For example, for CH_4 fuel at 800 °C, PPD of the modified cell drops to 0.36 W cm^{-2}, which is close to a PPD value of 0.34 W cm^{-2} with the conventional cell. When the temperature decreases to 750 °C, the conventional cell shows a slightly higher performance with a PPD of 0.20 W cm^{-2} compared with that of the modified cell with a PPD of 0.18 W cm^{-2}. The lower performance for the modified cell at low temperature is ascribed to the much lower catalytic activity of the catalyst layer for CH_4 steam reforming/oxidation at a lower temperature as shown in Fig. 4. The low catalytic activity reduces the H_2/CO production rate and leads to an insufficient fuel supply to generate power.

Fig. 6a and b present the I–$V(P)$ curves of cells with and without the LSCF catalyst layer using wet CH_4 and wet CBM at 850 °C, respectively. At low current density, the conventional cells show a higher loss than the modified cells with the LSCF catalyst layer. Because except for the independent catalyst layer, the materials and fabrication process of cells are identical, it is believed that the main difference in performance is ascribed to the anode side. A smaller electrode overpotential means a smaller anode overpotential, which reveals that most of the CH_4 fuel has been converted to CO and H_2 by the catalyst layer. Fig. 6c and d show the Nyquist plot and Bode plot of ESI for cells with and without the catalyst layer at 850 °C using 3% H_2O–97% CH_4 fuel. The modified cells with the LSCF catalyst layer exhibit
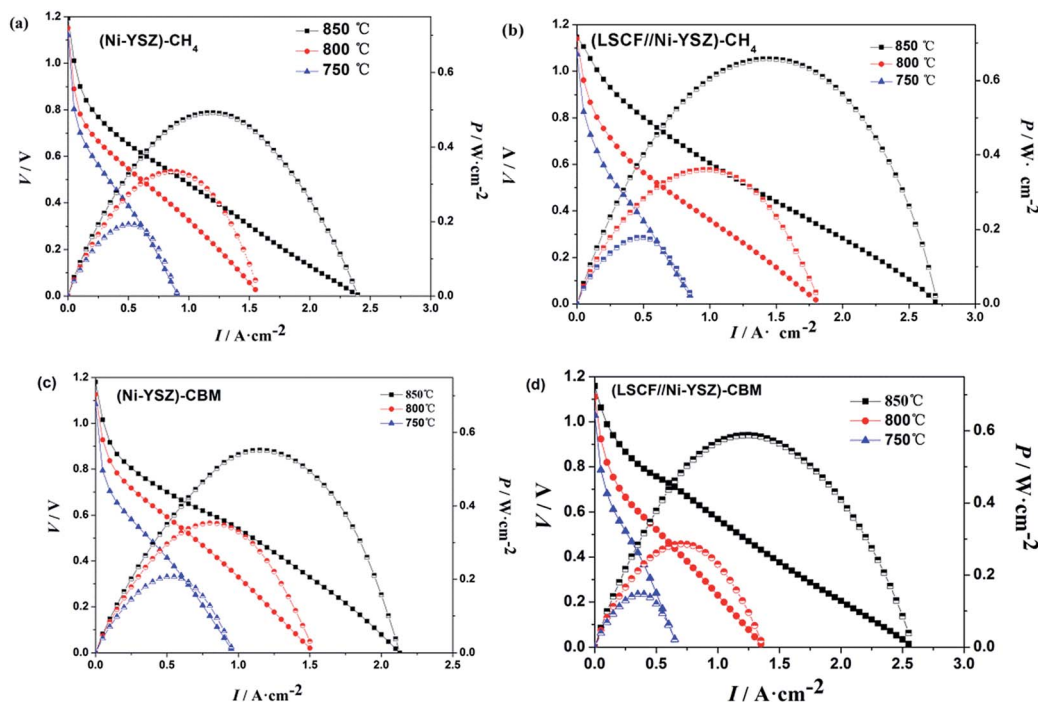

Fig. 5 Temperature-dependent polarization and power output for the conventional cell (a and c) and the modified cell with the LSCF catalyst layer (b and d) between 750 and 850 °C using 3% H_2O–97% CH_4 and 3% H_2O–97% CBM fuels, respectively.
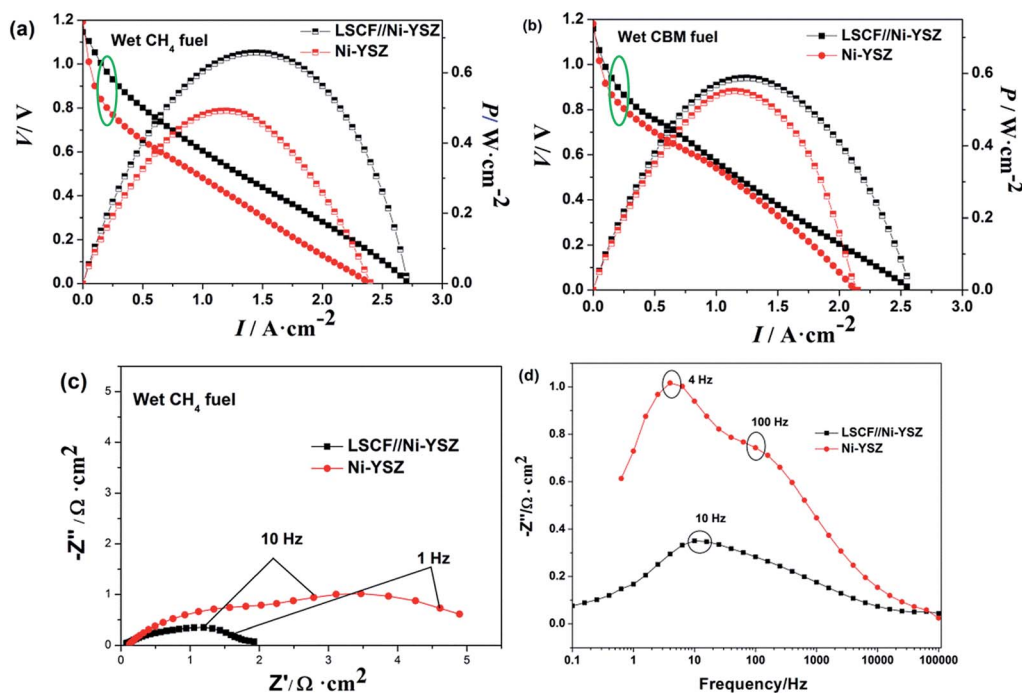
Fig. 6   Comparison of $I-V(P)$ for cells with and without the catalyst layer at 850 °C using 3% H_2O−97% CH_4 (a) and 3% H_2O−97% CBM fuels (b). The corresponding Nyquist plot (c) and Bode plot (d) of ESI for the two cells using 3% H_2O−97% CH_4.

a smaller polarization resistance (R_p) than the conventional cells, especially, the low-frequency resistance, which is related to a mass transfer limitation, suggesting a smaller mass transfer resistance compared with the conventional cell. The Bode plot is used to identify the rate determining step. The high-frequency domain is associated with the charge transfer process at the electrode/electrolyte interface; the low-frequency domain is related to the non-charge transfer process, including gas transport, adsorption–desorption of gas (O_2 and fuels), and surface diffusion of adsorbed gas species.

All processes are related to the overall impedance of the anode-supported cell, and it is difficult to identify the main factor responsible for the improved coking resistance without using an appropriate reference electrode. Since the two cells were fabricated with the same cell geometry, cathode and electrolyte, the difference in the Bode plot should be attributed to the changes in the anode. In Fig. 6d, the conventional cell exhibits higher impedance in the whole frequency domain than the modified cell, especially at frequencies lower than 1 kHz, which is in agreement with the increasing trend in impedance that is shown in the Nyquist plot, indicating that the application of the catalyst layer not only speeds up the charge transfer but also benefits adsorption and/or dissociation of fuels. The Bode plot shows two different processes within the conventional cell occurring at different frequencies: gas diffusion or gas conversion limitations[57] with a summit low frequency at 4 Hz; gas–solid interaction or the surface diffusion of the adsorbed species within the pores[57,58] with a medium frequency at 100 Hz. For the modified cell, the summit frequency at 10 Hz indicates that the reaction is dominated by mass-transfer limitations, probably caused by the barrier layer of the catalyst layer and the

complicated fuel composition including H_2, CO, CO_2, H_2O and CH_4. Applying a DC bias voltage (0.3 V) to the cells with and without the catalyst layer leads to the summit frequency shifting to a lower frequency, further indicating that the mass transfer or concentration polarization is the rate limiting process (Fig. S2†).

The electrochemical performance of the modified cells with the LSCF catalyst layer using H_2 fuel was used to provide a benchmark to prove the H_2-related electrochemical reaction when CH_4-based fuels are used. Fig. 7 shows the $I-V(P)$ curves measured in H_2, wet CH_4 and wet CBM at 850 °C. The cell fueled with CH_4 demonstrates an almost overlapping $I-V$ curve with the cell using H_2 fuel with an equal maximum load current of
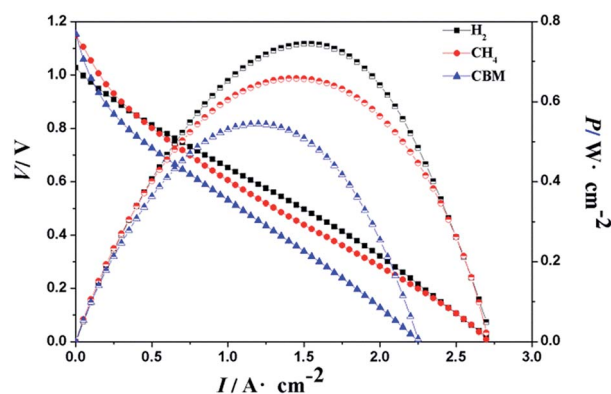

Fig. 7   Comparison of $I-V(P)$ for the modified cells with the LSCF catalyst layer at 850 °C using H_2, 3% H_2O−97% CH_4 and 3% H_2O−97% CBM fuels, respectively.

This journal is © The Royal Society of Chemistry 2016

J. Mater. Chem. A, 2016, 4, 13997–14007 | 14003

2.75 A. However, the cell fueled with CH_4 shows a slightly lower PPD than the cell using H_2 fuel, probably caused by a lower H_2 concentration because of the dilution effect of CO and CO_2. The cell using CBM fuel exhibits a ~9% PPD decrease compared with the cell using CH_4 fuel, probably because of the effect of heavy hydrocarbon compounds in CBM. It can be deduced that the catalyst has low catalytic activity for oxidation of heavy hydrocarbon compounds.

Discharge stability test at constant current density

Using 3% H_2O–97% CH_4 and 3% H_2O–97% CBM fuels, the voltage of the modified cells with an independent LSCF catalyst layer was monitored with time at a constant current density of 333 mA cm^{-2} at 800 °C (Fig. 8). For comparison, the conventional cell without the catalyst layer was also used. The voltage of the modified cell using CH_4 fuel stabilizes at 0.79 V with negligible degradation within 116 h compared to the conventional cell, which shows a significant voltage drop from 0.7 V to 0.1 V within 20 min. Using CBM fuel, the voltage of the modified cell exhibits a slow decrease within 12 h with a drop rate of 0.003 V h^{-1}, while the voltage of the conventional cell declines from 0.69 V to 0.43 V within 27 min. The voltage drop for the modified cell compared with that using the CH_4 cell is ascribed to the effect of heavy hydrocarbon compounds in CBM. This rapid voltage drop for the conventional cells is probably caused by the serious carbon deposition on the Ni cermet anode and the thermal–mechanical stress caused by local cooling within the anode due to the endothermic CH_4 reforming.[32] The good discharge stability using wet CH_4 fuel further indicates that the Ni cermet anode with the independent LSCF catalyst layer has a high coking resistance.

Post-test characterization of cells

Anode surface SEM images of the conventional cell and the modified cell with the LSCF catalyst layer after the discharge stability test using wet CH_4 fuel were investigated. It is clear that the conventional cell has many cracks (inset in Fig. 9a), while the modified cell with the LSCF catalyst layer remains intact after
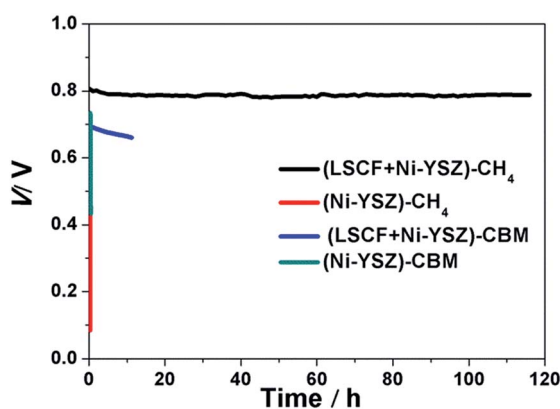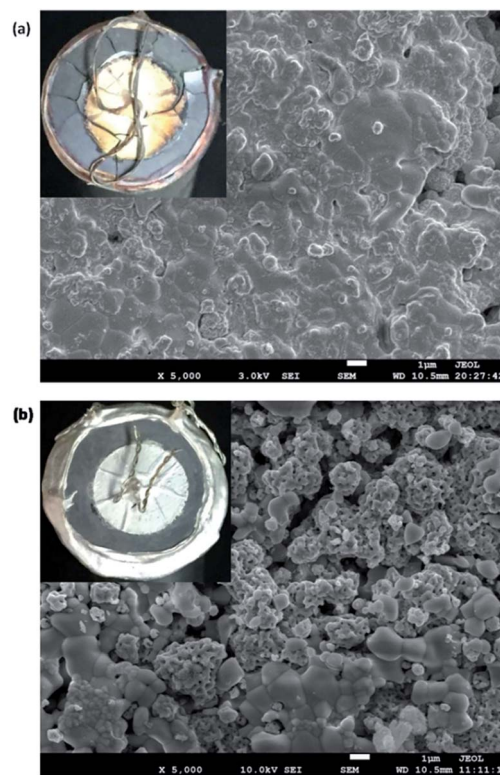

Fig. 9 SEM images of the anode surface of Ni−YSZ without (a) and with (b) the LSCF catalyst layer after the discharge stability test using wet CH_4 fuel.

Fig. 8 Time-dependent voltage of cells with and without a catalyst layer at a current density of 333 mA cm^{-2} at 800 °C using 3% H_2O–97% CH_4 and 3% H_2O–97% CBM fuels.

exposure to CH_4 for 116 h (inset in Fig. 9b). For the conventional cell, the anode surface showed a close-grained morphology accompanied by a few cracks (Fig. 9a). However, for the modified cell, thanks to the LSCF catalyst layer, after exposure to CH_4 fuel for 116 h, the anode and catalyst layer retain the granular texture with the porous morphology (Fig. 9b and 10b), ensuring the gas transportation. Clearly, LSCF particles show obvious sintering compared with that of a fresh surface (Fig. 10a). Although the modified cell with the LSCF catalyst layer using CBM fuel remains intact after exposure to CBM for 12 h, and many pores still remain in the catalyst layer, anode sintering happens obviously (Fig. S3†). This result indicates that the application of an independent LSCF catalyst layer greatly improves the coking resistance of the Ni cermet anode and reduces the thermal–mechanical stress within the anode when CH_4-based fuels are used.

EDX analysis of the anode surface of the modified cells and catalyst surface was carried out after the stability test in wet CH_4 and wet CBM (Fig. S4†). A long exposure to wet CH_4 leads to more carbon deposition. After 116 h, the total carbon content of the anode surface using CH_4 is about 4.62 wt%, more than 3.21 wt% of that after exposure to CBM for 12 h, while the total carbon contents on the LSCF catalyst surface using CH_4 and CBM are 2.74 wt% and 3.27 wt%. The low carbon content confirms that the independent LSCF catalyst layer can resist carbon deposition on the Ni particles. Probably the heavy carbon compounds in CBM lead to the slightly higher carbon content on the anode surface.
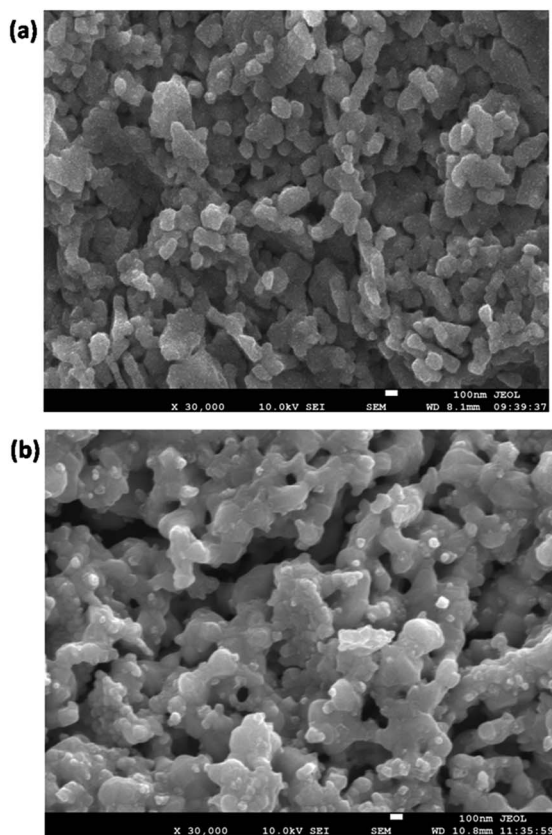
14004 | *J. Mater. Chem. A*, 2016, **4**, 13997–14007

This journal is © The Royal Society of Chemistry 2016

Fig. 10   SEM images of the LSCF catalyst layer surface before (a) and after (b) the discharge stability test using wet CH_4 fuel.

Discussions on the SOFC application of hydrocarbons based on the Ni cermet anode

Because of its high catalytic activity for hydrocarbon pyrolysis and the sufficient solubility for carbon, the Ni cermet anode suffers from coking when hydrocarbon fuels are used. In order to mitigate coking on the Ni cermet anode, usually a large amount of steam (steam to carbon ratio > 2) or CO_2 is applied to internally reform hydrocarbon fuels into H_2 and CO, which are not susceptible to coking. The CH_4-related reactions are shown in eqn (4) and (5):

$$CH_4 + H_2O = CO + 3H_2 \quad \Delta H^\circ_{298K} = +206 \ kJ \ mol^{-1} \quad (4)$$

$$CH_4 + CO_2 = 2CO + 2H_2 \quad \Delta H^\circ_{298K} = +247 \ kJ \ mol^{-1} \quad (5)$$

However, these two highly endothermic reforming reactions would lead to large temperature gradients across the anode, which causes cell cracking due to deleterious thermal–mechanical stresses. Furthermore, the temperature gradients along the anode increase with increasing methane conversion. Through analysis on anode surfaces in a 10 kW SOFC stack, Meusinger reported large temperature gradients along the Ni–YSZ cermet anode. For the case of S/C = 3, the minimum cermet temperature is 20 °C lower than at the beginning of the cermet.[30] Using IR thermometry, Meusinger measured a surface temperature difference of 30–35 °C between the anode entrance and exit during internal steam reforming of methane.[31] Pillai also indicated significant temperature gradients larger than 10 °C across the Ni–YSZ anode.[32] These large temperature variations are of great challenge for the structural and thermal stabilities of stack design.

Many strategies have been proposed to reduce coking on Ni-based anodes. For example, employing Ni with a less active metal such as Cu, Co, Sn or Au reduces the activity of Ni. Actually, the Ni-alloy significantly reduced coking on the Ni cermet anode, but did not eliminate it completely. Direct deposition of the catalyst functional layer over the anode surface also mitigates coking. However, the two above-mentioned strategies do not eliminate the thermal gradients across the anode because of the integrated structure of the catalyst and anode. In addition, functional materials must have a matching thermal expansion coefficient to avoid thermal stress that would cause cell cracking during thermal cycling of the SOFC. Catalytically active perovskite-type MIEC oxides have also been explored as SOFC anodes toward hydrocarbon applications, which function well without the need for excess steam or CO_2, thus thermal gradients are not major concerns. Nevertheless, the electronic conductivity of these materials is not sufficiently high under reducing conditions compared with the Ni cermet anode, which leads to lower cell performance. Therefore, Ni cermet anodes are still more prospective for practical application of hydrocarbon fuels.

Conclusion

Under SOFC conditions, a K_2NiF_4-type oxide (Sr,La)FeO_4 with CoFe alloy nanoparticles is formed *in situ*, which has high catalytic activity for methane oxidation/reforming. The homogeneous distribution of La, Sr, Co and Fe at the atomic level inside the LSCF oxide lattice ensures that the CoFe alloy is well dispersed. As an independent catalyst layer, the reduced product shows excellent coking resistance on the SOFC Ni cermet anode. The electrochemical performance of the modified cell is improved when 3% H_2O–97% CH_4 and 3% H_2O–97% CBM fuels are used. The cell assembly exhibits high coking resistance ability and good performance stability. The heavy hydrocarbon compounds present in CBM have a negative effect on cell performance, which indicates lower catalytic activity of the catalyst for heavy hydrocarbon oxidation. The application of an independent catalytic layer avoids damage to cells due to a large internal strain during the reduction of the catalyst, a thermal–mechanical stress from the mismatched thermal expansion coefficients between the catalyst and anode materials and the temperature variations caused by the endothermic reforming reaction of CH_4. Without large modification to the conventional SOFC based on the Ni cermet anode, this method provides a coking-free operation of SOFCs on practical methane-based fuels, therefore has a potential application prospect.

Acknowledgements

Notes and references

1 J. Jewulski, M. Skrzypkiewicz, M. Struzik and I. Lubarska-Radziejewska, *Int. J. Hydrogen Energy*, 2014, **39**, 21778–21785.

2 Y. Jiao, W. J. Tian, H. L. Chen, H. G. Shi, B. B. Yang, C. Li, Z. P. Shao, Z. P. Zhu and S. D. Li, *Appl. Energy*, 2015, **141**, 200–208.

3 Y. Jiao, J. H. Zhao, W. T. An, L. Q. Zhang, Y. J. Sha, G. M. Yang, Z. P. Shao, Z. P. Zhu and S. D. Li, *J. Power Sources*, 2015, **288**, 106–114.

4 A. S. Martinez, J. Brouwer and G. S. Samuelsen, *Appl. Energy*, 2015, **148**, 421–438.

5 M. Drewery, E. Kennedy, F. Alenazey, B. Dlugogorski and M. Stockenhuber, *Chem. Eng. Res. Des.*, 2015, **101**, 22–26.

6 B. W. Kwon, S. Z. Hu, Q. He, O. G. Marin-Flores, C. H. Oh, S. P. Yoon, J. Kim, J. Breit, L. Scudiero, M. G. Norton and S. Ha, *Appl. Catal., B*, 2015, **179**, 439–444.

7 H. Sumi, T. Yamaguchi, T. Suzuki, H. Shimada, K. Hamamoto and Y. Fujishiro, *J. Ceram. Soc. Jpn.*, 2015, **123**, 213–216.

8 L. Zhang, C. H. Yang, A. I. Frenkel, S. W. Wang, G. L. Xiao, K. Brinkman and F. L. Chen, *J. Power Sources*, 2014, **262**, 421–428.

9 A. A. Al-Musa, Z. S. Ioakeimidis, M. S. Al-Saleh, A. Al-Zahrany, G. E. Marnellos and M. Konsolakis, *Int. J. Hydrogen Energy*, 2014, **39**, 19541–19554.

10 C. Su, Y. B. Chen, W. Wang, R. Ran, Z. P. Shao, J. C. D. da Costa and S. M. Liu, *Environ. Sci. Technol.*, 2014, **48**, 7122–7127.

11 W. Wang, C. Su, R. Ran, B. T. Zhao, Z. P. Shao, M. O. Tade and S. M. Liu, *ChemSusChem*, 2014, **7**, 1719–1728.

12 Y. F. Sun, J. H. Li, L. Cui, B. Hua, S. H. Cui, J. Li and J. L. Luo, *Nanoscale*, 2015, **7**, 11173–11181.

13 B. Hua, M. Li, W. Y. Zhang, J. Pu, B. Chi and L. Jian, *J. Electrochem. Soc.*, 2014, **161**, F569–F575.

14 W. Wang, H. Y. Zhu, G. M. Yang, H. J. Park, D. W. Jung, C. Kwak and Z. P. Shao, *J. Power Sources*, 2014, **258**, 134–141.

15 Y. M. Park and H. Kim, *Int. J. Hydrogen Energy*, 2014, **39**, 16513–16523.

16 D. Yoon and A. Manthiram, *J. Mater. Chem. A*, 2015, **3**, 21824–21831.

17 Z. T. Tao, G. H. Hou, N. Xu and Q. F. Zhang, *Int. J. Hydrogen Energy*, 2014, **39**, 5113–5120.

18 M. V. Sandoval, A. Matta, T. Matencio, R. Z. Domingues, G. A. Ludwig, M. D. Korb, C. D. Malfatti, P. Gauthier-Maradei and G. H. Gauthier, *Solid State Ionics*, 2014, **261**, 36–44.

19 M. Li, B. Hua, J. L. Luo, S. P. Jiang, J. Pu, B. Chi and L. Jian, *J. Mater. Chem. A*, 2015, **3**, 21609–21617.

20 T. Nagasawa and K. Hanamura, *J. Therm. Sci. Technol.*, 2015, **10**, JTST0011, DOI: 10.1299/jtst.2015jtst0011.

21 C. H. Yang, J. Li, Y. Lin, J. Liu, F. L. Chen and M. L. Liu, *Nano Energy*, 2015, **11**, 704–710.

22 Y. F. Sun, J. H. Li, K. T. Chuang and J. L. Luo, *J. Power Sources*, 2015, **274**, 483–487.

23 T. S. Oh, A. S. Yu, L. Adijanto, R. J. Gorte and J. M. Vohs, *J. Power Sources*, 2014, **262**, 207–212.

24 C. Aliotta, L. F. Liotta, F. Deganello, V. La Parola and A. Martorana, *Appl. Catal., B*, 2016, **180**, 424–433.

25 J. Mirzababaei and S. S. C. Chuang, *Catalysts*, 2014, **4**, 146–161.

26 S. E. Evans, J. Z. Staniforth, R. J. Darton and R. M. Ormerod, *Green Chem.*, 2014, **16**, 4587–4594.

27 K. Zheng, K. Swierczek, J. M. Polfus, M. F. Sunding, M. Pishahang and T. Norby, *J. Electrochem. Soc.*, 2015, **162**, F1078–F1087.

28 J. S. Yoon, E. J. Yi, B. H. Choi, M. J. Ji and H. J. Hwang, *Ceram. Int.*, 2014, **40**, 1525–1529.

29 W. Wang, C. Su, Y. Z. Wu, R. Ran and Z. P. Shao, *Chem. Rev.*, 2013, **113**, 8104–8151.

30 J. Meusinger, E. Riensche and U. Stimming, *J. Power Sources*, 1998, **71**, 315–320.

31 J. E. A. Saunders and M. H. Davy, *Int. J. Hydrogen Energy*, 2013, **38**, 13762–13773.

32 M. Pillai, Y. B. Lin, H. Y. Zhu, R. J. Kee and S. A. Barnett, *J. Power Sources*, 2010, **195**, 271–279.

33 W. An, D. Gatewood, B. Dunlap and C. H. Turner, *J. Power Sources*, 2011, **196**, 4724–4728.

34 I. V. Zagaynov, A. S. Loktev, A. L. Arashanova, V. K. Ivanov, A. G. Dedov and I. I. Moiseev, *Chem. Eng. J.*, 2016, **290**, 193–200.

35 P. Li, Y. C. Zhao, B. L. Yu, J. Li and Y. D. Li, *Int. J. Hydrogen Energy*, 2015, **40**, 9783–9789.

36 H. Kim, C. Lu, W. L. Worrell, J. M. Vohs and R. J. Gorte, *J. Electrochem. Soc.*, 2002, **149**, A247–A250.

37 C. H. Yang, Z. B. Yang, C. Jin, G. L. Xiao, F. L. Chen and M. F. Han, *Adv. Mater.*, 2012, **24**, 1439–1443.

38 S. Miyoshi, T. Furuno, H. Matsumoto and T. Ishihara, *Solid State Ionics*, 2006, **177**, 2269–2273.

39 L. F. Zhang, Y. P. Wang and Q. W. Huang, *Trans. Nonferrous Met. Soc. China*, 2009, **19**, 1444–1449.

40 V. V. Kharton, E. V. Tsipis, E. N. Naumovich, A. Thursfield, M. V. Patrakeev, V. A. Kolotygin, J. C. Waerenborgh and I. S. Metcalfe, *J. Solid State Chem.*, 2008, **181**, 1425–1433.

41 G. M. Yang, C. Su, Y. B. Chen, M. O. Tade and Z. P. Shao, *J. Mater. Chem. A*, 2014, **2**, 19526–19535.

42 M. Ghouse, Y. Al-Yousef, A. Al-Musa and M. F. Al-Otaibi, *Int. J. Hydrogen Energy*, 2010, **35**, 9411–9419.

43 L. M. P. Garcia, D. A. Macedo, G. L. Souza, F. V. Motta, C. A. Paskocimas and R. M. Nascimento, *Ceram. Int.*, 2013, **39**, 8385–8392.

44 W. X. Liu, Z. Zhao, B. F. Tu, D. A. Cui, D. R. Ou and M. J. Cheng, *Int. J. Hydrogen Energy*, 2015, **40**, 4861–4867.

45 B. Wei, K. F. Chen, C. C. Wang, Z. Lu and S. P. Jiang, *Solid State Ionics*, 2015, **281**, 29–37.

46 A. Kulkarni, F. T. Ciacchi, S. Giddey, C. Munnings, S. P. S. Badwal, J. A. Kimpton and D. Fini, *Int. J. Hydrogen Energy*, 2012, **37**, 19092–19102.

47 T. Luo, X. J. Liu, X. Meng, H. Wu, S. R. Wang and Z. L. Zhan, *J. Power Sources*, 2015, **299**, 472–479.

14006 | *J. Mater. Chem. A*, 2016, **4**, 13997–14007

This journal is © The Royal Society of Chemistry 2016

48 B. Hua, M. Li, J. L. Luo, J. Pu, B. Chi and J. Li, *J. Power Sources*, 2016, **303**, 340–346.

49 Y.-S. Chou, M.-H. Huang, N.-Y. Hsu, K.-T. Jeng, R.-Y. Lee and S.-C. Yen, *Int. J. Hydrogen Energy*, 2016, **41**, 12953–12961.

50 V. Kyriakou, I. Garagounis, A. Vourros, E. Vasileiou, A. Manerbino, W. G. Coors and M. Stoukides, *Appl. Catal., B*, 2016, **186**, 1–9.

51 L. N. Bobrova, V. A. Sadykov, N. V. Mezentseva, V. V. Pelipenko, N. V. Vernikovskaya, O. P. Klenov and O. L. Smorygo, *Int. J. Hydrogen Energy*, 2016, **41**, 4632–4645.

52 J. F. Qu, W. Wang, Y. B. Chen, X. Deng and Z. P. Shao, *Appl. Energy*, 2016, **164**, 563–571.

53 Y. S. Chung, H. Kim, H. C. Yoon, J. S. Chung and N. M. Sammes, *Fuel Cells*, 2015, **15**, 416–426.

54 T. W. Kim, J. C. Park, T. H. Lim, H. Jung, D. H. Chun, H. T. Lee, S. Hong and J. I. Yang, *Int. J. Hydrogen Energy*, 2015, **40**, 4512–4518.

55 P. S. Roy, N. K. Park and K. Kim, *Int. J. Hydrogen Energy*, 2014, **39**, 4299–4310.

56 N. Bogolowski, B. Iwanschitz and J. F. Drillet, *Fuel Cells*, 2015, **15**, 711–717.

57 A. Bertei, G. Arcolini, J. P. Ouweltjes, Z. Wuillemin, P. Piccardo and C. Nicolella, *Electrochim. Acta*, 2016, **208**, 129–141.

58 H. P. Dasari, S. Y. Park, J. Kim, J. H. Lee, B. K. Kim, H. J. Je, H. W. Lee and K. J. Yoon, *J. Power Sources*, 2013, **240**, 721–728.